

System Identification Modeling of a Small-Scale Unmanned Rotorcraft for Flight Control Design



Bernard Mettler
*The Robotics Institute
Carnegie Mellon University
Pittsburgh, PA*



Mark B. Tischler
*Aeroflightdynamics Directorate (AMRDEC)
US Army Aviation and Missile Command
Ames Research Center, CA*



Takeo Kanade
*The Robotics Institute
Carnegie Mellon University
Pittsburgh, PA*

This paper describes the development of a parameterized model for a small-scale unmanned helicopter (Yamaha R-50 with 10 ft rotor diameter) and its identification using a frequency domain identification technique. The model explicitly accounts for the stabilizer bar, which has a strong influence on the flight dynamics characteristics. The accuracy of the identified model is verified by comparing the model-predicted responses with the responses collected during flight experiments. Furthermore, the values of key identified parameters are compared with the values predicted by helicopter theory to show that the model has a physically meaningful parameterization. Both hover and cruise flight conditions are examined.

Nomenclature

a, b	longitudinal and lateral rotor flapping angles
c, d	longitudinal and lateral stabilizer bar flapping angles
K_d	stabilizer bar gearing
N	scale factor; helicopter with $1/N$ -th rotor diameter
p, q, r	roll, pitch, and yaw rates in helicopter reference frame
u, v, w	longitudinal, lateral, and vertical speed in helicopter reference frame
δ_{col}	collective control input
δ_{lat}	cyclic lateral control input
δ_{lon}	cyclic longitudinal control input
δ_{ped}	directional control input
γ	blade Lock number
γ_{eff}	effective Lock number
γ_{yu}	coherence function between system input u and output y
τ_f	main rotor time constant
τ_s	stabilizer bar time constant

Introduction

Small-scale helicopters are increasingly popular platforms for unmanned aerial vehicles (UAVs). The ability of helicopters to take off and land vertically, to perform hover flight as well as cruise flight, and their agility, makes them ideal vehicles for a range of applications in a variety of environments. Existing small-scale rotorcraft-based UAVs (RUAVs), however, exploit only a modest part of the helicopter's inherent qualities. For example, their operation is generally limited to hover and slow-speed flight, and their control performance is, in most cases, sluggish. These limitations on RUAV operation are mainly due to flight control systems that are designed without precise knowledge of the vehicle dynamics.

Throughout the 1990s, most RUAVs used classical control systems such as single-input-single-output proportional-derivative (PD) feedback

control systems. Their controller parameters were usually tuned empirically. For more advanced multivariable controller synthesis approaches, an accurate model of the dynamics is required. Such models, however, are not readily available and are difficult to develop.

The dynamic models used for controller synthesis or controller optimization have strict requirements. The model must capture the effects that govern the performance and maneuverability of the vehicle. High-bandwidth multivariable control requires models with high-bandwidth accuracy. For helicopters, this implies that such a model must explicitly account for effects such as the rotor-fuselage coupling. At the same time, however, the model must be simple enough to be insightful and practical for the controller synthesis.

Using a standard modeling approach based on first principles, considerable knowledge of rotorcraft flight dynamics is required, and comprehensive flight validations and model refinements are necessary to attain sufficient accuracy. System identification represents an attractive alternative and has already been used successfully for full-scale helicopters (Refs. 1, 2).

A few examples of the application of system identification techniques to the modeling of small-scale helicopters exist. The results obtained are limited compared with what is regularly achieved with full-scale helicopters. For example, as shown in Ref. 3, to support model-based control design, the authors identified the rigid-body angular dynamics of the vehicle using measurements collected from a rigged helicopter. In another example (Ref. 4), the authors developed a simulation model to evaluate various control strategies. They identified the vertical-longitudinal aircraft dynamics, with second-order pitch angle dynamics, from flight data collected on a free-flying helicopter.

This paper describes the first comprehensive application of system identification techniques to a small-scale helicopter. Carnegie Mellon's autonomous Yamaha R-50 helicopter (Ref. 5), shown in Fig. 1, is used to conduct the experiments. A complete parameterized model describing the dynamics of the vehicle about its six degrees of freedom is developed. The model includes the rotor and stabilizer bar dynamics, which allow for improved high-bandwidth fidelity and, at the same time, for the



Fig. 1. Instrumented R-50 in hovering flight.

extraction of important physical parameters. The Comprehensive Identification from Frequency Responses (CIFER) is used to identify the parameterized model (Ref. 1). Both the hover and cruise flight conditions are modeled. Subsequently, the model is successfully validated by comparing the model-predicted responses with the responses collected during flight experiments. Finally, the values of key identified parameters are compared with the values predicted by rotorcraft theory (Ref. 6) to demonstrate that the parameterization is consistent with the physical characteristics of the small-scale rotorcraft.

Description of the Test Vehicle

Yamaha R-50 helicopter

The Yamaha R-50 helicopter is a commercial small-scale helicopter originally developed for remotely operated crop dusting. Figure 2 and Table 1 show some of its physical characteristics.

The R-50 uses a two-bladed main rotor with a Bell-Hiller stabilizer bar. The head has a tri-hinge configuration; the two blades are attached

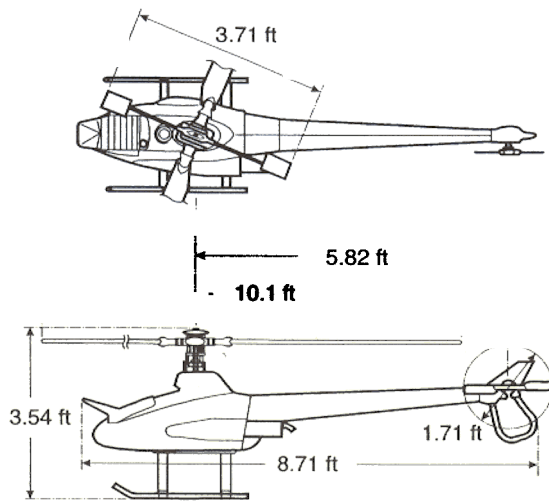


Fig. 2. Dimensions of the Yamaha R-50 helicopter.

Table 1. Physical characteristics of the Yamaha R-50

Rotor speed	850 rpm
Tip speed	449 ft/s
Dry weight	97 lb.
Instrumented	150 lb.
Engine	Single cylinder, 2-stroke
Flight autonomy	30 minutes

to a yoke through individual flapping hinges, and the yoke is connected to the rotor shaft through a teetering hinge. All the hinges are restrained by elastomeric fittings.

The Bell-Hiller stabilizer bar performs the role of a stability augmentation system. It is essentially a secondary rotor consisting of a pair of paddles connected to the rotor shaft by an unrestrained teetering hinge. The stabilizer bar receives the same lateral and longitudinal cyclic control inputs as the main rotor; however, owing to its proportionally smaller aerodynamic surface and larger moment of inertia, the stabilizer bar has a slower response than the main rotor, and is less sensitive to airspeed and wind gust disturbances. The stabilizer bar flapping motion is added to the main rotor cyclic control through a mechanical mixer. This produces a lagged rate (or “pseudo-attitude”) feedback in the pitch and roll loops, stabilizing the low frequency dynamics and increasing the phase margin for pilot/vehicle system in the crossover frequency range (1–3 rad/sec) (Ref. 7).

Scaling considerations

Stabilizer bars are common in small-scale helicopters. The reason is that the scaling down of helicopters increases not only their sensitivity to control inputs and disturbances, but also the bandwidth of their dynamics, and thus makes them harder to control.

A key effect in rotorcraft dynamics is the damping that the rotor provides for the roll and pitch motion. The rotor-induced damping arises from the tendency of the rotor—therefore of the thrust vector—to lag behind the shaft during pitching or rolling motions. This lag, which is a function of the rotor time constant τ_f , produces a moment about the helicopter’s center of gravity opposite to the rolling or pitching direction and proportional to the rolling or pitching rate.

Smaller helicopters have a higher rotor speed. For a scale ratio N (refers to a helicopter with $1/N$ -th rotor diameter), a Froude scale model (similar ratio of inertial to gravitational forces, i.e., enforces dynamic similarity (Ref. 8)) has a \sqrt{N} times faster rotor speed. A Mach scale model (similar blade tip speed as a full-scale helicopter, allowing faster airspeed than Froude scale models) has a N times faster rotor speed. Since the rotor time constant is inversely proportional to the rotor speed Ω ($\tau_f = 16/\gamma\Omega$, where γ is the nondimensional blade Lock number), the rotor of a small-scale rotorcraft has a smaller time constant and, thus produces less damping. This increases the roll or pitch rate sensitivity (defined as the ratio of control sensitivity to rotor damping (Ref. 9)). The rate sensitivity is \sqrt{N} times higher for a Froude-scale model and N times higher for a Mach-scale model.

Onboard instrumentation

Carnegie Mellon’s RUAV instrumentation is designed to produce high quality flight data. The centerpiece of the helicopter onboard system is a flight computer which hosts a Motorola 68060 processor board and a sensor input/output (I/O) board. All sensors and actuators of the helicopter connect through the I/O board with the exception of the inertial measurement unit (IMU), which connects directly to the processor board through a special serial port. Telemetry to the ground station takes place via wireless Ethernet.

The RUAV uses three navigation sensors: 1) a fiber-optic inertial measurement unit (IMU), which provides measurements of the airframe accelerations a_x, a_y, a_z , and angular rates p, q, r (resolution: 0.002 g and 0.0027 deg/sec, data rate: 400 Hz); 2) a dual frequency differential global positioning system (GPS) (precision: 2 cm, update rate: 4 Hz); and 3) a magnetic compass for heading information (resolution: 0.5 degrees, update rate: 2 Hz).

The IMU is installed on the side of the aircraft, the GPS and the compass on the tail. Velocity and acceleration measurements are corrected for the offset between the position of the helicopter center of gravity and the positions of the sensors. A Kalman filter running at 100 Hz integrates the measurements from the IMU, GPS and compass to produce accurate estimates of helicopter position, velocity and attitude.

Rotor speed is maintained by an engine governor. Three linear servo-actuators are used to control the swashplate, while another actuator is used to control the collective pitch of the tail rotor. The dynamics of all the actuators are identified from data collected during ground experiments. The swashplate actuators is approximated with a first-order transfer function:

$$G_s(s) = \frac{15}{s + 15} \quad (1)$$

The dynamics of the tail rotor actuator are identified, together with the dynamics of the yaw rate gyro, and are presented later.

Frequency-Domain System Identification

For the system identification, Comprehensive Identification from FrEQUENCY Responses (CIFER) analysis tool is used. CIFER was developed specifically for rotorcraft, and has been successfully used on a number of full-scale rotorcraft (Refs. 1, 2, 10, 11).

Frequency responses fully describe the linear dynamics of a system. When the system has nonlinear dynamics (to some extent all real physical systems have them), system identification determines the describing functions which are the best linear fit of the system response based on a first harmonic approximation of the complete Fourier series.

In frequency domain identification, the parameters of an *a priori*-defined model are adjusted to minimize a cost function that measures the fit between the frequency responses derived from data collected from the system and the frequency responses predicted by the model. A comprehensive description of CIFER is given in Ref. 1.

The goal of system identification is to achieve the best possible fit of the flight data with a model that is consistent with the physical knowledge of the vehicle dynamics. The first part of the problem consists of the development of the parameterized dynamic model. Once accomplished, the values of the model parameters can be identified. Based on the accuracy attained, the model structure is then refined until satisfactory results are achieved.

The criteria used for this iteration are: i) level of frequency response agreement (frequency error costs), ii) statistical metrics from the model parameters (insensitivity and Cramer-Rao percent), iii) agreement of the system's time responses (time domain verification), and iv) agreement of the identified key physical parameters with their theoretical values.

Flight Testing: Collection of Flight Data

High quality flight data are essential to a successful identification. The principal concerns are the accuracy of the estimated vehicle states, the information content of the flight data (i.e., whether the measurements contain evidence of the relevant vehicle dynamics), and the compatibility of the flight data with the postulate of linear dynamics used for modeling. While the accuracy of the estimated vehicle states depends on instrumentation, the information content and compatibility depend to a large extent on the execution of the flight experiments.

A useful metric to verify that the flight data are satisfactory for the purpose of system identification is the coherence function (Ref. 12). The coherence function γ_{xy} (or partial coherence for a multiple-input multiple-output system) indicates how well the output y (any of the estimated helicopter states) is linearly correlated with a particular input x over the examined frequency range. It is computed together with the system's fre-

quency responses, from the cross spectrum G_{xy} , and the input and output auto-spectra G_{xx} and G_{yy} , respectively (note that the partial coherence is derived from the conditioned spectrum); the mathematical definition is

$$\gamma_{yu}^2 = \frac{|G_{yu}|^2}{G_{uu}G_{yy}} \leq 1 \quad (2)$$

A value of 0.6 for the coherence function is usually used as a limit. For lower coherence values the identified frequency responses will have a too-high random error. A low coherence can be attributed to: poor signal-to-noise ratio, nonlinearities in the dynamics, or the presence of unmeasured inputs such as wind gusts.

The coherence function helps develop and refine the parameterized model. For example, it indicates which outputs are influenced by each control input. Also, the frequency range can provide cues about the nature of the physical effects. Specifically, the coherence serves as a weighting function in the frequency domain cost function, which is used to identify the model parameters.

Flight-test procedure

Low frequency excitations are important for the identification of the speed derivatives (0.1–1 rad/sec), and high frequency excitations are important for the identification of the coupled rotor/fuselage dynamics (8–14 rad/sec). To guarantee that the flight data capture the dynamics, a frequency-sweep technique is used, where the pilot gradually increases the frequency of the input (Ref. 10).

The experiments were conducted open-loop except for an active yaw damping system. A block-diagram representation of the augmented R-50 dynamics is shown in Fig. 3. Note that the stabilizer bar can also be regarded as a dynamic augmentation (feedback gains K_c and K_d). An input cross-feed K_f is used by Yamaha between the collective input and the directional input to compensate for coupling effects between the heave and yaw dynamics.

Two series of flight experiments were organized for each hover and cruise condition. For each flight in a series, the pilot applied a frequency sweep control sequence to one of the four control inputs via the remote control (RC) unit. While doing so, the pilot used the other control inputs to maintain the helicopter within the selected operating condition. The same experiment was repeated several times to gather sufficient data. Figure 4 shows a sample of filtered flight data of the longitudinal and lateral vehicle axes for two concatenated lateral frequency sweeps conducted in hover.

The inputs to the system are the four helicopter control inputs (cyclic longitudinal δ_{lon} and lateral δ_{lat} , cyclic collective δ_{col} and directional δ_{ped}) which enter the system via four actuators (three swashplate actuators G_s and one tail actuator G_T). The outputs are the rigid-body fuselage states: translational velocities u, v, w and angular velocities p, q, r .

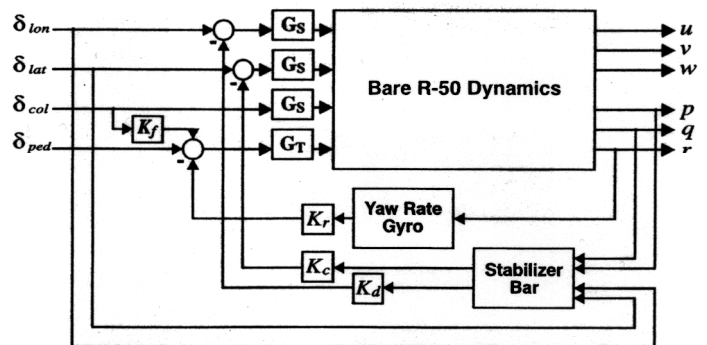


Fig. 3. Block-diagram showing the interconnection between the bare R-50 airframe and the components of the augmented airframe.

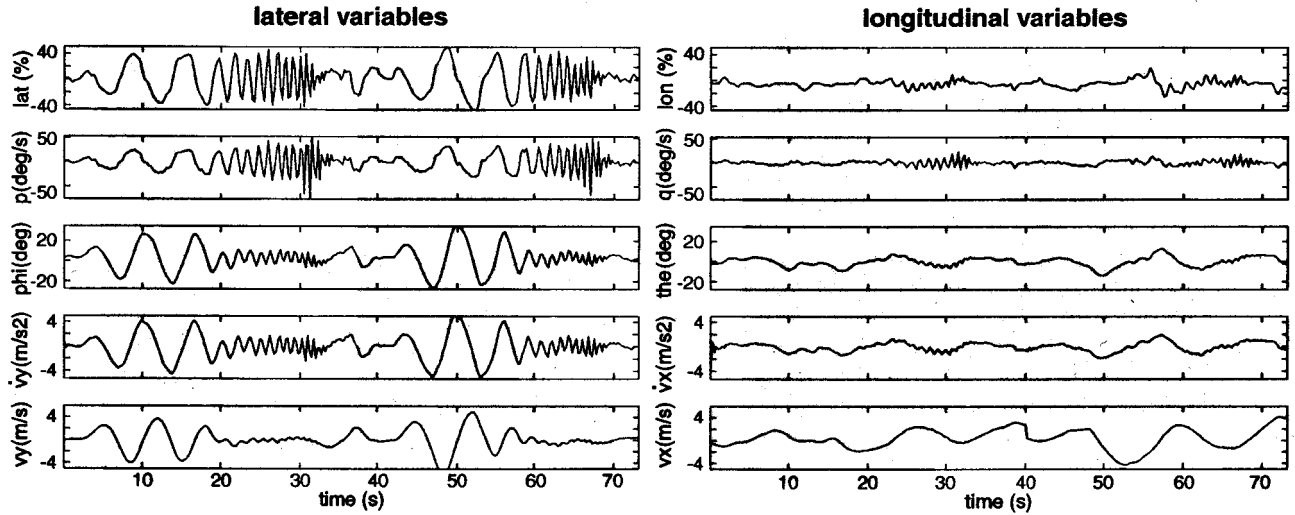


Fig. 4. Time histories from sample flight data collected during a frequency sweep applied to the lateral cyclic.

Both the yaw damping system and the stabilizer bar (see Fig. 5) are represented as dynamic augmentations. All control inputs (stick inputs) and all helicopter states were recorded (100 Hz sampling rate). Flight data from the best runs were then concatenated and filtered ($-3 \text{ dB @ } 10 \text{ Hz}$) to remove undesired information such as structural vibrations.

The collection of flight data in cruise condition was challenging because the helicopter was moving and the pilot relied only on visual cues to control the aircraft. This made it difficult to collect long flight data sequences. The record length t_{rec} is critical because it determines the lowest frequency that can be extracted from the flight data ($\omega_{min} = 2\pi/t_{rec}$). A fly-over technique was used: that is, the pilot accelerated the R-50 for a constant distance until it reached a speed that was comfortable for the pilot. The pilot then performed the control sweeps while trying to maintain a constant airspeed. Increasing the record length made it more difficult for the pilot to maintain a constant airspeed. By allowing the airspeeds to vary between 30 and 60 ft/sec (10 and 20 m/sec), a maximum record length of 10 sec was achieved.

Frequency response analysis

The frequency responses derived from the hover-flight data with the calculated coherence metrics are depicted in Fig. 6. All on-axis responses attained a coherence close to unity over the frequency range where the relevant dynamical effects take place. For example, the two on-axis angular rate responses to their respective cyclic inputs achieve a good coherence (≥ 0.6) from 0.32 rad/sec up to the frequencies of 8–16 rad/sec, where the important fuselage/rotor coupling takes place.

The frequency responses and coherence functions derived from cruise flight are depicted in Fig. 7. Here again, all the on-axis responses achieved high coherence values (here only from 0.64 rad/sec because of the short flight data sequences). The generally high coherence obtained for the key helicopter responses also indicates that the vehicle dynamics are predominantly linear for the test conditions.

The frequency responses and coherence functions give important cues about the characteristics of the vehicle dynamics. Good examples are the angular responses (roll rate p and pitch rate q) to the cyclic inputs (lateral input δ_{lat} and longitudinal input δ_{lon}). The corresponding frequency responses (Figs. 6 and 7), show that the vehicle’s roll and pitch dynamics have a well defined lightly-damped second-order nature. This characteristic is visible in both the on- and off-axis responses. Second-order responses are typical of dynamically coupled systems, as a result of coupling between the airframe angular motion and the regressive rotor flap

dynamics (blade flapping a , b). The light damping is due to the presence of the stabilizer bar (Ref. 7).

Development of the Parameterized Model

The basic equations of motion for a linear model of helicopter dynamics are derived from the Newton-Euler equations for a rigid body that is free to rotate and translate simultaneously in all six degrees of freedom. The external aerodynamic and gravitational forces are represented in a stability derivative form. In the simplest model, no additional states are used, and the control forces produced by the main rotor and tail rotor are expressed by the multiplication of a control derivative and the corresponding control input.

However, a key aspect of helicopter dynamics is the dynamical coupling between the main rotor (which produces most of the control forces and moments) and the helicopter fuselage. Omitting this coupling effect has been shown to limit the accuracy of the helicopter model in the medium to high frequency range (Ref. 13). Therefore, for high-bandwidth control design, or for accurate handling quality evaluations, it is essential to account for the dynamic coupling between the rotor and the fuselage. Such an accounting requires that the rotor dynamics are modeled explicitly and then coupled to the fuselage equations of motions. A standard way to achieve this is the hybrid-model formulation originally developed for full-scale helicopter modeling (Ref. 1). Other effects involving additional dynamics sometimes need to be accounted for as well, including the actuators, the engine/drive train system, and control augmentation (such as the active yaw damping system or the stabilizer bar). A more refined structure also yields a model that is physically more consistent; i.e., the identified values have a better defined physical meaning.

Lateral and longitudinal fuselage dynamics

The four equations for the translational and angular fuselage motions are derived from the Newton-Euler equations:

$$\dot{u} = (-w_0q + v_0r) - g\theta + X_u u + \dots + X_a a \quad (3)$$

$$\dot{v} = (-u_0r + w_0p) - g\phi + Y_v v + \dots + Y_b b \quad (4)$$

$$\dot{p} = L_u u + L_v v + \dots + L_b b \quad (5)$$

$$\dot{q} = M_u u + M_v v + \dots + M_a a \quad (6)$$

The external aerodynamic and gravitational forces and moments are formulated in terms of stability derivatives (Ref. 6). For example, the rotor forces are expressed through the rotor derivatives X_a , Y_b , and the rotor moments through the flapping spring-derivatives L_b , M_a . General aerodynamic effects are expressed by speed derivatives such as X_u , Y_v , L_u , L_v , M_u , M_v . The centrifugal terms in the linear-motion equations, which are a function of the trim condition (u_0 , v_0 , w_0), are relevant only in cruise flight.

Coupled rotor/stabilizer bar dynamics

The rotor dynamics are represented as a first order tip-path-plane model. This representation, which is obtained by simplifying the coupled second-order blade flapping equations (Ref. 14), has been used in most full-scale rotorcraft identifications (Ref. 1). The simplified rotor model consists of two first-order differential equations for the lateral (b) and longitudinal (a) flapping motions:

$$\tau_f \dot{b} = -b - \tau_f p - B_a a + B_{lat} \delta_{lat} + B_{lon} \delta_{lon} \quad (7)$$

$$\tau_f \dot{a} = -a - \tau_f q + A_b b + A_{lat} \delta_{lat} + A_{lon} \delta_{lon} \quad (8)$$

where τ_f is the main rotor time constant; B_{lat} , B_{lon} and A_{lat} , A_{lon} are the stick to swashplate gearings; B_a and A_b are cross-coupling derivatives.

In the initial application of system identification to the modeling of the R-50 (Ref. 15), the stabilizer bar was not explicitly modeled. The resulting model allowed a good fit of the flight data; however, the identified parameters did not provide a good insight into the effects of the stabilizer bar. To address this limitation, the rotor model is expanded to include the equations of motion for the stabilizer bar flapping.

The stabilizer bar is regarded as a secondary rotor attached to the rotor shaft above the main rotor through an unrestrained teetering hinge (see Fig. 5). The blades consist of two paddles. The stabilizer bar receives cyclic inputs from the swash-plate in a similar way as do the main blades. Because of the teetering hinge and the absence of restraint, the stabilizer bar is less subject to cross axis effects than the main rotor. The tip-path plane model used is the same as for the main rotor but in an uncoupled form; see Eqs. (7) and (8). The equations for the lateral (d) and longitudinal (c) flapping motions are

$$\tau_s \dot{d} = -d - \tau_s p + D_{lat} \delta_{lat} \quad (9)$$

$$\tau_s \dot{c} = -c - \tau_s q + C_{lon} \delta_{lon} \quad (10)$$

where τ_s is the stabilizer bar time constant; D_{lat} and C_{lon} are the stick to swashplate gearings.

The stabilizer bar is assumed not to exert any forces or moments on the shaft. The bar dynamics are coupled to the main rotor via the Bell mixer (see Fig. 5). The Bell mixer is a mechanical mixer, which

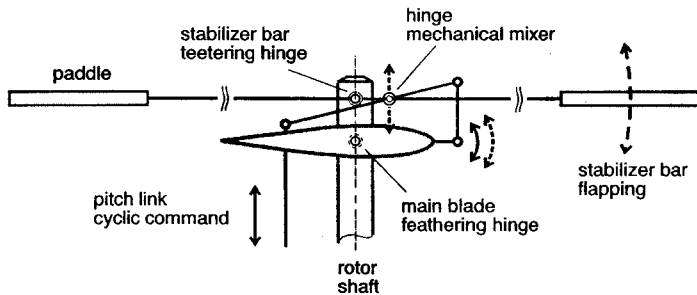


Fig. 5. Rotor-stabilizer mechanization. (The main blade pitch control receives both the cyclic pitch command and a component that is proportional to the stabilizer bar flapping angle. The cyclic pitch augmentation is implemented through a mechanical mixer.)

superposes a cyclic command proportional to the amount of stabilizer bar flapping to the cyclic commands coming from the swashplate. The resulting augmented lateral and longitudinal main rotor cyclic commands can be written:

$$\bar{\delta}_{lat} = \delta_{lat} + K_d d \quad \text{and} \quad \bar{\delta}_{lon} = \delta_{lon} + K_c c \quad (11)$$

The derivatives K_d and K_c represent the gearing of the stabilizer bar Bell-mixer, which are functions of the mixer's geometry. Applying the Laplace transformation to the stabilizer bar lateral flapping equations (Eqs. (9) and (10)) yields

$$d = -\frac{p}{s + 1/\tau_s} + \frac{D_{lat}/\tau_s}{s + 1/\tau_s} \delta_{lat} \quad (12)$$

which shows that the stabilizer bar can be modeled as a lagged rate feedback.

Substituting the augmented cyclic commands, typified by Eq. (11), in the main rotor equations of motion, typified by Eqs. (7) and (8), the following result is obtained:

$$\tau_f \dot{b} = -b - \tau_f p + B_a a + B_{lat}(\delta_{lat} + K_d d) + B_{lon} \delta_{lon} \quad (13)$$

$$\tau_f \dot{a} = -a - \tau_f q + A_b b + A_{lat} \delta_{lat} + A_{lon}(\delta_{lon} + K_c c) \quad (14)$$

In the final state-space model, the control augmentation is determined using the system's states. Thus, the following derivatives are defined: $B_d = B_{lat} K_d$ and $A_c = A_{lon} K_c$. These derivatives and the gearing of the Bell-mixer are related:

$$K_d = \frac{B_d}{B_{lat}} \quad \text{and} \quad K_c = \frac{A_c}{A_{lon}} \quad (15)$$

In reality, since the Bell-mixer behavior is independent of rotor azimuth, the gearing is the same for both the axes. The gearing value is determined experimentally. These relations of Eq. (15) could have been used as a constraint between the derivatives B_{lat} and B_d (A_{lon} and A_c) to reduce the number of unknown parameters. However, owing to the uncertainty of how to approach the modeling of the stabilizer bar, the derivatives are left free. (The identified value is compared to the value obtained experimentally later in the paper.)

Heave dynamics

The frequency response of the vertical acceleration to the collective pitch input for the hover-flight conditions (az/col in Fig. 6), shows that a first-order system adequately captures the heave dynamics. This agrees with the Newton-Euler rigid body equations:

$$\dot{w} = (-v_0 p + u_0 q) + Z_w w + Z_{col} \delta_{col} \quad (16)$$

The term in parentheses corresponds to the centrifugal forces that become relevant in cruise flight conditions.

Note that the az/col frequency response does not exhibit the peak in magnitude caused by the inflow effects typical of full-size helicopters. (The changes in induced velocity at the rotor in response to changes in the blade pitch are, in reality, not instantaneous; this aerodynamic lag results in a dynamic coupling between the blade flapping motion and the surrounding air.) For the R-50, this effect is not visible because its flap frequency ($1/rev = 89$ rad/sec) is well beyond the frequency range of identification and of piloted excitation (30–40 rad/sec).

Yaw dynamics

The yaw dynamics of the bare helicopter airframe can be modeled as a simple first order system:

$$\frac{r}{\delta_{ped}} = \frac{N_{ped}}{s - N_r} \quad (17)$$

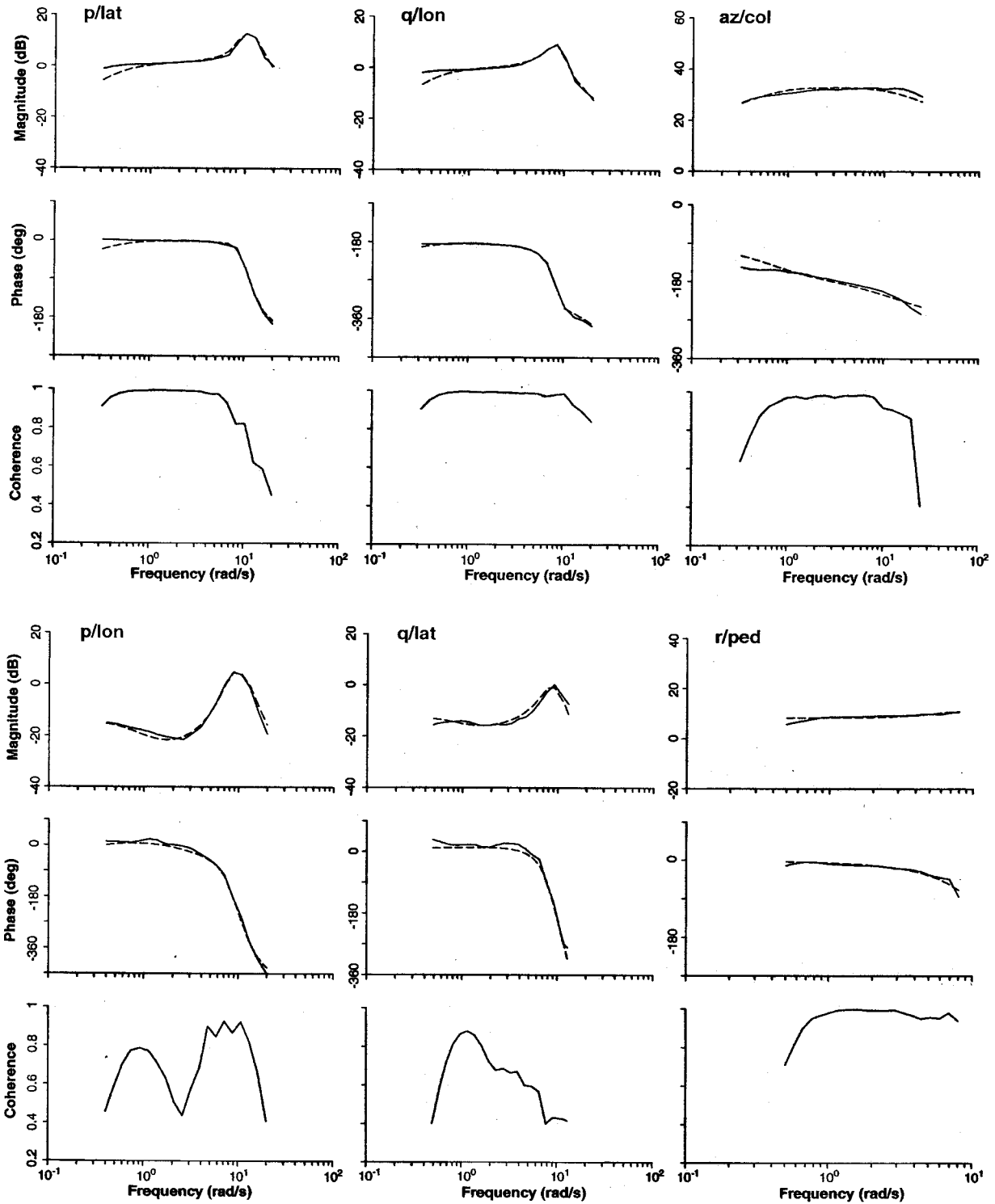


Fig. 6. Comparison between the frequency responses computed from the flight data (solid) and those derived from the identified model (dashed); the results are for the hover flight condition.

where N_r is the bare airframe yaw damping coefficient and N_{ped} is the sensitivity to the directional control. However, the artificial yaw damping system used during the flight testing necessitates an explicit formulation of its effect on the yaw dynamics.

The artificial yaw damping is achieved through feedback of the helicopter yaw rate. Since, at the time of the flight experiment, only the pilot directional input δ_{ped} and the helicopter yaw rate r were measured, ground experiments were performed to isolate the dynamics of the tail

actuator and yaw rate gyro. The dynamics of the actuator and rate gyro are described by their respective frequency responses H_{act} and H_{gyro} . By expressing the unknown yaw dynamics of the bare airframe as the frequency response $H_{r\delta}$, the frequency response of the augmented yaw dynamics is formulated from the closed-loop transfer function:

$$T_{r\delta, aug} = \frac{H_{r\delta} H_{act}}{1 + H_{r\delta} H_{act} H_{gyro}} \quad (18)$$

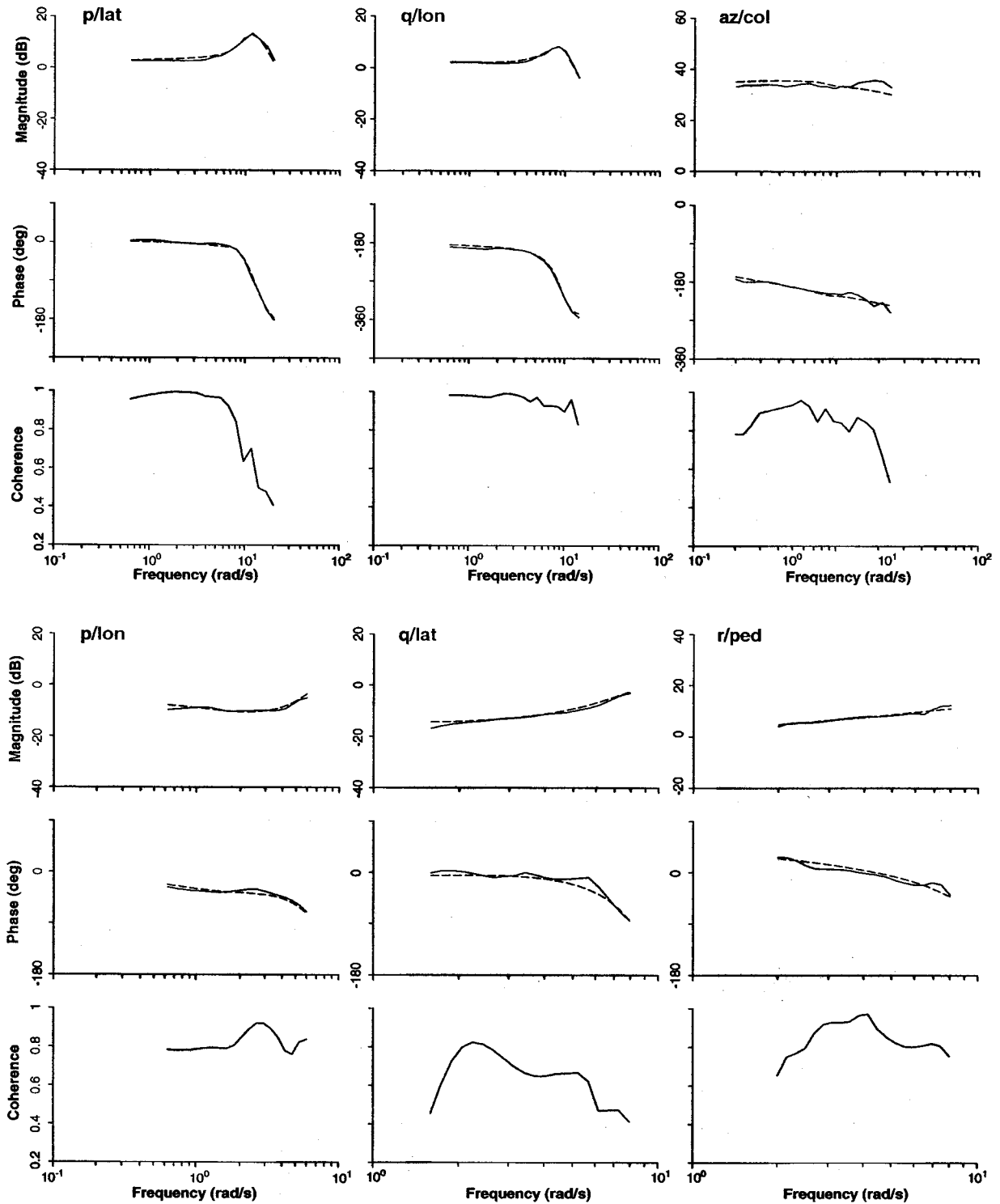


Fig. 7. Comparison between the frequency responses computed from the flight data (solid) and those derived from the identified model (dashed); the results are for the cruise flight condition.

Since the frequency response of $T_{r\delta, aug}$ is known from the flight experiments, the frequency response of the unknown bare airframe dynamics $H_{r\delta}$ is evaluated from the frequency response arithmetic:

$$H_{r\delta} = \frac{H_{r\delta, aug}}{H_{act} - H_{r\delta, aug} H_{act} H_{gyro}} \quad (19)$$

The resulting frequency response for the bare airframe yaw dynamics $H_{r\delta}$ does not exhibit the first order form of Eq. (17). From this, it is concluded that other dynamic effects, such as the engine drive-train dynamics, influence the yaw dynamics.

To avoid increasing the complexity of the model, it is decided to revert to the representation used in Ref. 15. That is, the augmented yaw dynamics is approximated as a first-order bare airframe dynamics with a yaw rate feedback represented by a simple first-order low-pass filter:

$$\begin{bmatrix} \dot{u} \\ \dot{v} \\ \dot{p} \\ \dot{q} \\ \dot{\phi} \\ \dot{\theta} \\ \tau_f \dot{a} \\ \tau_f \dot{b} \\ \dot{w} \\ \dot{r} \\ \dot{r}_{fb} \\ \tau_s \dot{c} \\ \tau_s \dot{d} \end{bmatrix} = \begin{bmatrix} X_u & 0 & 0 & 0 & 0 & -g & X_a & 0 & 0 & 0 & 0 & 0 & 0 & 0 \\ 0 & Y_v & 0 & 0 & 0 & g & 0 & Y_b & 0 & 0 & 0 & 0 & 0 & 0 \\ L_u & L_v & 0 & 0 & 0 & 0 & 0 & L_b & L_w & 0 & 0 & 0 & 0 & 0 \\ M_u & M_v & 0 & 0 & 0 & 0 & M_a & 0 & M_w & 0 & 0 & 0 & 0 & 0 \\ 0 & 0 & 1 & 0 & 0 & 0 & 0 & 0 & 0 & 0 & 0 & 0 & 0 & 0 \\ 0 & 0 & 0 & 1 & 0 & 0 & 0 & 0 & 0 & 0 & 0 & 0 & 0 & 0 \\ 0 & 0 & 0 & -\tau_f & 0 & 0 & -1 & A_b & 0 & 0 & 0 & A_c & 0 & 0 \\ 0 & 0 & -\tau_f & 0 & 0 & 0 & B_a & -1 & 0 & 0 & 0 & 0 & B_d & 0 \\ 0 & 0 & 0 & 0 & 0 & 0 & Z_a & Z_b & Z_w & Z_r & 0 & 0 & 0 & 0 \\ 0 & N_v & N_p & 0 & 0 & 0 & 0 & 0 & N_w & N_r & N_{r_{fb}} & 0 & 0 & 0 \\ 0 & 0 & 0 & 0 & 0 & 0 & 0 & 0 & 0 & K_r & K_{r_{fb}} & 0 & 0 & 0 \\ 0 & 0 & 0 & -\tau_s & 0 & 0 & 0 & 0 & 0 & 0 & 0 & -1 & 0 & 0 \\ 0 & 0 & -\tau_s & 0 & 0 & 0 & 0 & 0 & 0 & 0 & 0 & 0 & 0 & -1 \end{bmatrix} \begin{bmatrix} u \\ v \\ p \\ q \\ \phi \\ \theta \\ a \\ b \\ w \\ r \\ r_{fb} \\ c \\ d \end{bmatrix} + \begin{bmatrix} 0 & 0 & 0 & 0 \\ 0 & 0 & Y_{ped} & 0 \\ 0 & 0 & 0 & 0 \\ 0 & 0 & 0 & M_{col} \\ 0 & 0 & 0 & 0 \\ 0 & 0 & 0 & 0 \\ A_{lat} & A_{lon} & 0 & 0 \\ B_{lat} & B_{lon} & 0 & 0 \\ 0 & 0 & 0 & Z_{col} \\ 0 & 0 & N_{ped} & N_{col} \\ 0 & 0 & 0 & 0 \\ 0 & C_{lon} & 0 & 0 \\ D_{lat} & 0 & 0 & 0 \end{bmatrix} \begin{bmatrix} \delta_{lat} \\ \delta_{lon} \\ \delta_{ped} \\ \delta_{col} \end{bmatrix}$$

Fig. 8. Parameterized state-space model.

$$\frac{r_{fb}}{r} = \frac{K_r}{s + K_{r_{fb}}} \quad (20)$$

$$u_m = u + h_{cg}q \quad (25)$$

$$v_m = v - h_{cg}p \quad (26)$$

The closed loop transfer function for the augmented yaw rate response becomes

With this method, it is possible to enforce the constraint $-X_a = Y_b = g$ and, at the same time, identify the unknown vertical offset h_{cg} .

$$\frac{r}{\delta_{ped}} = \frac{N_{ped}(s + K_{r_{fb}})}{s^2 + (K_{r_{fb}} - N_r)s + (K_r N_{ped} - N_r K_{r_{fb}})} \quad (21)$$

Identification of the Model Parameters

And the corresponding differential equations used in the state-space model are

The full state-space model of the R-50 dynamics is obtained by collecting all the differential equations in a matrix form:

$$\dot{r} = N_r r + N_{ped}(\delta_{ped} - r_{fb}) \quad (22)$$

$$M\dot{x} = Fx + Gu \quad (27)$$

$$\dot{r}_{fb} = -K_{r_{fb}}r_{fb} + K_r r \quad (23)$$

Again, since the pilot input δ_{ped} and the yaw rate r are the only measurements, the above representation is over-parameterized. One constraint between two parameters must be added to avoid having problems during the identification because of correlated parameters. It is, therefore, stipulated that the pole of the low-pass filter must be twice as fast as the pole of the bare airframe yaw dynamics:

where x is the state vector and u is the input vector. The system matrix F contains the stability derivatives; the input matrix G contains the input derivatives; and the M matrix contains the rotor time constants for the rotor flapping equations. The full state-space system is depicted in Fig. 8. The frequency responses used for the state-space identification are selected from the coherence measure obtained during the multivariable frequency domain analysis; see Table 2. The final structure is obtained by adding and removing derivatives according to the quality of the frequency domain fit and statistical information about the derivatives. The useful statistics are the insensitivity of the cost function to each derivative and the correlation between the derivatives. Insensitive and/or correlated parameters are dropped.

$$K_{r_{fb}} = -2N_r \quad (24)$$

With this constraint, a low transfer function cost is attained. The value obtained for the bare airframe yaw damping N_r , is not necessarily and physically meaningful. However, this should not constitute a limitation, since the active yaw damping system can be retained in future flight control designs as part of the bare airframe dynamics.

A helicopter responds differently in hover flight than it does in cruise flight. However, it is observed that in this case, these differences does not significantly affect the model structure. For the cruise-flight condition the centrifugal acceleration terms that appear in the equations of motion of the fuselage's translational accelerations must be accounted for; that is, Eqs. (3), (4), and (16). The average trim condition for the cruise-flight experiments is $u_0 = 49.2$ ft/sec, $v_0 = -11$ ft/sec, and $w_0 = 0$ ft/sec.

Flight-data kinematics

In the lateral and longitudinal translations, typified by Eqs. (3) and (4), the derivatives X_a and Y_b should theoretically be equal, respectively, to plus and minus the value of gravity ($g = 32.1$ ft/sec²). Enforcing that constraint is possible only if the flight data has been properly corrected for the position offset in the sensor location relative to the center of gravity (C.G.). Since, in the present case, the C.G. location is not known with sufficient accuracy, vertical offset h_{cg} is explicitly accounted for by relating the measured speeds (u_m, v_m) to the speed at the C.G. (u, v) as follows:

The differences between the hover and cruise conditions are seen in Table 2, which shows the frequency ranges that are selected for the identification, and in the actual identified model parameters. The largest change occurs in the lateral-directional behavior (weather-vane speed derivative N_v). Other changes are discussed next.

Table 2. Frequency responses and frequency ranges selected for the identification process. (First row: hover condition; second row: cruise flight condition). Notice that not all input-output pairs are used

	δ_{lat}	δ_{lon}	δ_{col}	δ_{ped}
p	0.32–20 0.7–20	0.4–20 0.7–14	- 2.4–16	- -
q	0.4–20 1.6–10	0.32–20 0.7–20	- 0.7–18	- -
r	0.4–1.6 0.7–11	- -	0.7–3 -	0.5–8 -
a_x	0.4–8	0.32–14 0.7–12	- -	- -
a_y	0.32–20 0.7–10	- -	- -	- -
a_z	3–16 0.7–5	6–16 0.7–24	0.32–30 -	4–8 -
u	0.4–8 -	0.32–14 -	- -	- -
v	0.32–16 0.63–9	0.4–16 -	- -	- -
w	- 1.4–9	- 0.63–12	- -	- -

Results and Discussion

Frequency response agreement

The predicted frequency responses from the identified model agree well with the frequency responses from the flight-data in both hover and cruise conditions. The transfer function costs are given in Table 3 and the frequency response comparison is depicted in Figs. 6 and 7. Compared with the results obtained for the lumped rotor/stabilizer bar (Ref. 15), the off-axis angular responses (p to δ_{lon} and q to δ_{lat}) are significantly improved by explicitly modeling the stabilizer bar (costs: 37 vs. 101 and 50 vs. 100, respectively).

This close agreement is better than what is usually achieved for full-scale helicopters where an average cost of 70 is considered excellent. This is due to the dynamics of small-scale rotorcraft being governed by first-order effects. In particular, the rotor forces and moments clearly dominate the vehicle dynamics, as demonstrated by the distinctly second-order characteristic of the roll and pitch dynamics.

Identified model parameters

Tables 4 and 5 give the values of the identified derivatives as well as two statistical metrics: the Cramer-Rao percent (CR%) and the insensitivity (Insens.%). The values of these metrics indicate that all of the key control and response parameters are extracted with a high degree of precision (Ref. 10). Notice that most of the quasi-steady derivatives are dropped, thus showing that the rotor forces dominate the dynamics of small-scale helicopters. This dominance is also reflected by the number of rotor flapping derivatives (\cdot)_b and (\cdot)_a. The term *actuated helicopter* is a good idealization of the dynamics of the small-scale helicopter, where the rotor dominates the response.

Rotor parameters. The identified stabilizer-bar and main-rotor time constants for the hover conditions are $\tau_s = 0.34$ sec and $\tau_f = 0.046$ sec, respectively. These values are close to the theoretical values of

Table 3. Transfer function costs attained for each input-output pair during the identification

	Hover	Cruise
v_x/lat	15.7	-
v_y/lat	18.4	-
v_z/lat	-	71.1
p/lat	61.5	13
q/lat	50.4	18.5
a_x/lat	15.7	-
a_y/lat	17.4	23.5
r/lat	27.4	-
a_z/lat	25	-
v_x/lon	27.9	-
v_y/lon	35	-
v_z/lon	-	48.5
p/lon	37.1	15.6
q/lon	41.3	9.7
a_x/lon	27.9	48.8
a_y/lon	35	-
a_z/lon	33.8	44.2
p/col	-	45.8
q/col	-	19.1
r/col	35.2	-
a_z/col	55.3	78.2
a_y/ped	-	10.3
v_y/ped	-	39.1
r/ped	18.8	23.5
a_z/ped	19.4	-
Average	31.5	33.9

$\tau_s = 0.36$ sec and $\tau_f = 0.053$ sec, predicted from the stabilizer-bar and main rotor Lock number γ , and the rotor speed Ω . That is,

$$\tau = \frac{16}{\gamma\Omega} \quad (28)$$

The blade Lock number describes the ratio between the aerodynamic and inertial forces acting on the blade:

$$\gamma = \frac{\rho c_b c_\alpha (R^4 - r^4)}{I_\beta} \quad (29)$$

It is defined by air density ρ , blade chord length c_b , lift curve slope c_α , inside and outside radii of the blade r , and R , and blade inertia I_β .

For the hover condition, the main blade Lock number is corrected for the inflow effects (Ref. 11). The effective Lock number is

$$\gamma_{\text{eff}} = \frac{\gamma}{1 + c_\alpha \sigma / 16 v_0} \quad (30)$$

where σ is rotor solidity, and v_0 is inflow ratio derived from the thrust coefficient ($v_0 = \sqrt{0.5c_T}$). These results also validate the results from the earlier work (Ref. 15), where the main rotor and stabilizer bar were modeled as a lumped system. It can now be stated that the time constants identified at the time ($\tau = 0.38$ sec) belonged to the stabilizer bar. This identification shows that the stabilizer bar dominates the rotor response. In cruise condition the rotor time constants decrease to $\tau_s = 0.26$ sec and $\tau_f = 0.035$ sec.

Coupling derivatives. The stabilizer bar couples to the main rotor through the derivatives B_d and A_c . Application of Eq. (15), gives the equivalent Bell-mixer gearing. The results of $K_d = 10.92$ and $K_c = 12.88$ for, respectively, the lateral and longitudinal axes, are close to the real gearing $K = 13.58$ determined experimentally. In forward flight, the

Table 4. Identified model parameters for hover- and cruise-flight conditions—Part I

	Hover Flight			Cruise Flight			Ratio
	Value	CR %	Insens. %	Value	CR %	Insens. %	
M-Matrix							
τ_f	0.046	10.9	1.64	0.0346	31.7	2.37	0.75
h_{log}	-0.411	6.25	1.78	-0.321	14.7	6.695	0.78
τ_s	0.342	7.35	0.828	0.259	6.52	0.786	0.76
F-Matrix							
X_u	-0.0505	62.3	29.6	-0.122	57.7	27.5	2.41
X_θ, X_α	-32.2	constrained to $-g$		-32.2	constrained to $-g$		-
X_r	-	-	-	-11	centrifugal term, constrained to v_0		-
Y_v	-0.154	22.9	10.9	-0.155	32.7	6.84	1
Y_ϕ, Y_β	32.2	constrained to $-g$		32.2	constrained to $-g$		-
Y_r	-	-	-	-49.2	centrifugal term, constrained to $-u_0$		-
L_u	-0.144	12.3	3.07	-	-	-	-
L_v	0.143	19.5	6.54	-	-	-	-
L_w	-	-	-	-0.213	15.3	3.96	-
L_b	166	1.87	0.6	213	0.00145	2.14	1.28
M_u	-0.0561	20.2	5.63	-	-	-	-
M_v	-0.0585	14.5	4.23	-	-	-	-
M_w	-	-	-	0.0728	21.2	5.68	-
M_α	82.6	6.28	0.592	108	0.0593	0.786	1.31
B_α	0.368	10.5	1.13	0.419	11.5	2.18	1.14
B_β	0.71	4.11	0.782	0.664	9.66	1.55	0.93
A_b	-0.189	11.7	4.47	-0.176	21.9	9.39	0.93
A_c	0.644	9.49	0.819	0.577	7.73	1.09	0.89
Z_b	-131	2.77	1.62	-	-	-	-
Z_α	-9.75	19.9	8.26	-	-	-	-

Table 5. Identified model parameters for hover- and cruise-flight conditions—Part II

	Hover Flight			Cruise Flight			Ratio
	Value	CR %	Insens. %	Value	CR %	Insens. %	
F-Matrix (cont.)							
Z_w	-0.614	10.5	4.47	-1.01	4.72	2.07	1.65
Z_r	0.93	8.15	2.75	-	-	-	-
Z_p	-	-	-	11	centrifugal term, constrained to $-v_0$		-
Z_q	-	-	-	49.2	centrifugal term, constrained to u_0		-
N_p	-3.53	14.2	3.66	-	-	-	-
N_v	0.0301	32.5	9.08	0.401	8.8	3.36	13.3
N_w	0.0857	14.1	5.09	-	-	-	-
N_r	-4.13	9.71	2.79	-3.9	10.6	3.67	0.94
$N_{r_{fb}}$	-33.1	$N_{r_{fb}} = -N_{ped}$		-26.4	$N_{r_{fb}} = -N_{ped}$		0.8
K_r	2.16	4.42	1.74	2.18	7.75	2.7	1
$K_{r_{fb}}$	-8.26	$K_{r_{fb}} = 2N_r$		-7.79	$K_{r_{fb}} = 2N_r$		0.94
G-Matrix							
B_{lat}	0.14	7.06	1.61	0.124	16.3	2.64	0.88
B_{lon}	0.0138	13.4	4.21	0.02	17.8	6.7	1.45
A_{lat}	0.0313	7.89	2.06	0.0265	8.19	2.54	0.85
A_{lon}	-0.1	9.21	1.18	-0.0837	13.9	1.87	0.83
Z_{col}	-45.8	4.32	1.84	-60.3	4.06	1.86	1.31
M_{col}	-	-	-	6.98	6	1.43	-
N_{col}	-3.33	10.6	3.67	-	-	-	-
N_{ped}	33.1	5.45	1.92	26.4	7.18	2.44	0.8
D_{lat}	0.273	12.2	1.89	0.29	12.5	2.36	1.06
C_{lon}	-0.259	10.7	1.62	-0.225	11.2	1.66	0.87
Y_{ped}	-	-	-	11.23	21.9	4.66	-
τ_{ped}	0.0991	13.2	6.09	0.0589	21.8	6.93	0.59

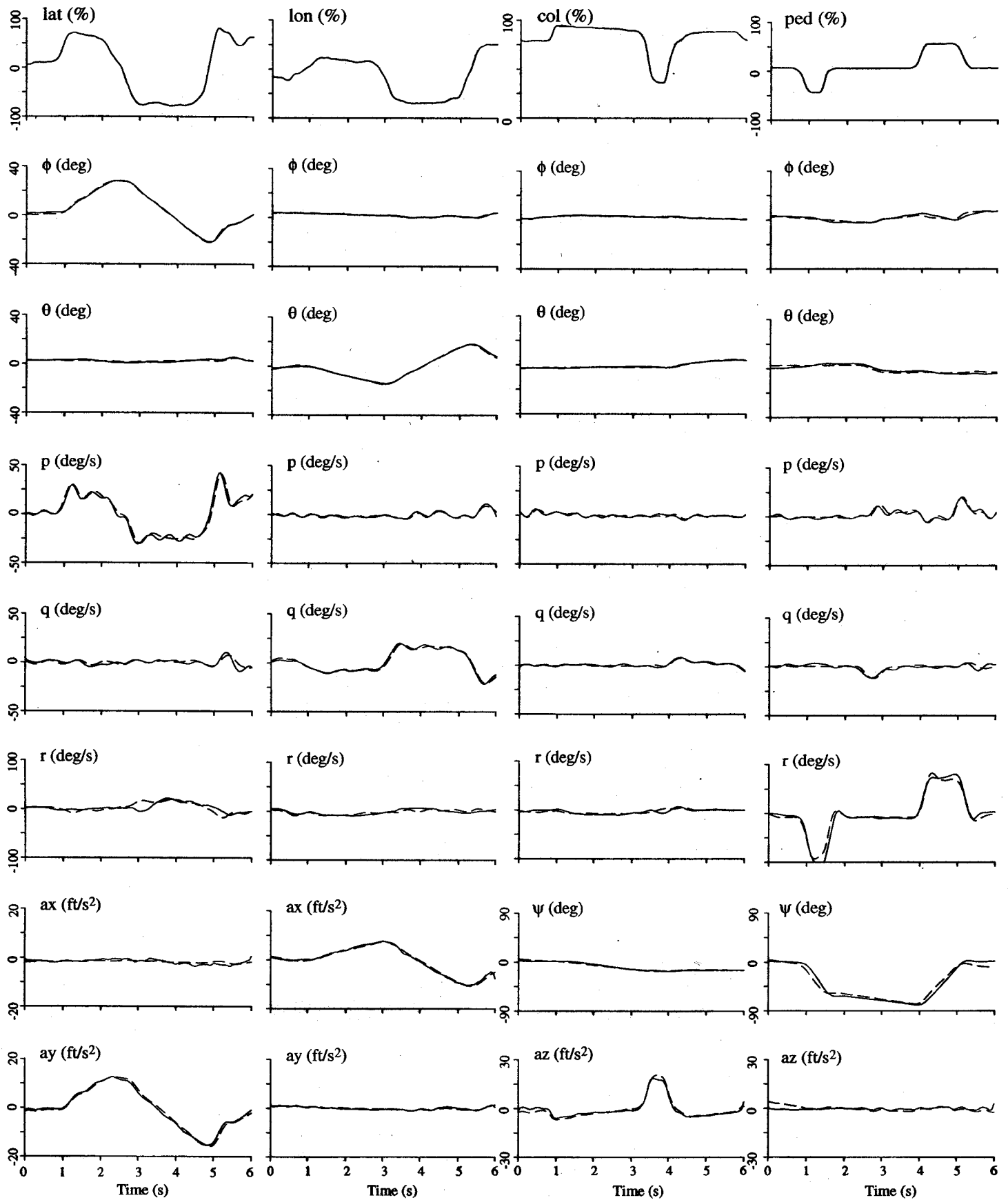


Fig. 9. Comparison between the responses predicted by the identified hover model (dashed) and the responses obtained during flight testing in hover condition (solid).

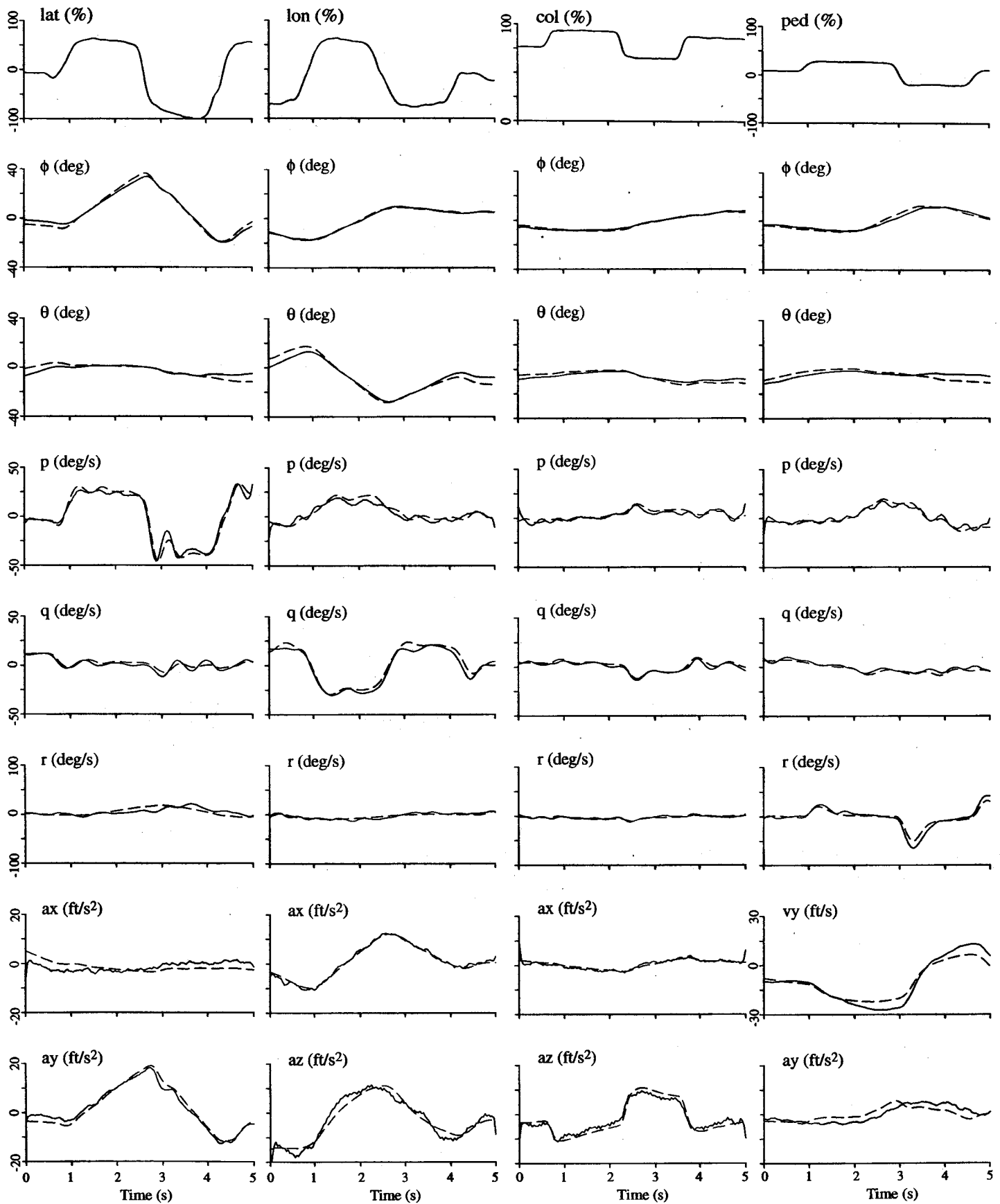


Fig. 10. Comparison between the responses predicted by the identified cruise model (dashed) and the responses obtained during flight testing in cruise condition (solid).

equivalent gearing results are: $K_d = 10.73$ and $K_c = 13.79$, and agree with the reality that the gearing is a mechanical constant. The identified roll and pitch rotor spring derivatives are, respectively, $L_b = 166.1$ and $M_a = 82.57$, for hover conditions. These values for cruise conditions are about 30% larger: $L_b = 213.2$ and $M_a = 108$. The lateral and longitudinal main rotor control derivatives have reasonable values with only slight changes between hover and cruise conditions. The only exception is B_{lon} , which is 45% larger in cruise flight, indicating a higher cross axis activity. The stabilizer bar control derivatives are almost identical for both flight conditions. These physically meaningful results indicate that the hybrid model structure with the stabilizer bar augmentation accurately captures the coupled fuselage/rotor/stabilizer bar dynamics.

Quasi-steady and speed derivatives. The speed derivatives X_u , and Y_v , in the translational equations, Eqs. (3) and (4), have the sign and relative magnitudes expected for a hovering helicopter, but the absolute magnitudes are all considerably larger (2–5 times) than those for full scale aircraft. This is expected since the weight of the small-scale helicopters is proportionally smaller (weight scales by $1/N^3$). In cruise flight, the longitudinal speed derivative X_u increases significantly. Note that this derivative has the highest insensitivity of all the derivatives (29.6 and 27.5 for, respectively, hover and cruise flight), as well as a very high Cramer-Rao values. Therefore, the identified value is unreliable. This weak result is due to the insufficient low-frequency information content of the flight data caused by the short flight-data sequences (10 sec).

The speed derivatives L_u , L_v , M_u and M_v in angular rate equations, Eqs. (5) and (6), contribute a destabilizing influence on the phugoid dynamics. These derivatives are dropped for the cruise conditions because of excessive Cramer-Rao values.

With the help of the offset Equations (25) and (26), the force coupling derivatives are constrained to gravity ($-X_a = Y_b = g$). At the same time, the vertical C.G offset is identified to be $h_{cg} = -0.41$ ft for hover and $h_{cg} = -0.32$ ft for cruise. The small difference of 0.09 ft (2.7 cm) is due to changes in configuration and other unmodeled factors.

Yaw dynamics. Little can be said with regard to the yaw dynamics because of the approximations used. Note that the yaw damping has the correct negative sign, and that the yaw rate feedback coefficients stay virtually constant between hover and cruise conditions. The major changes are those affecting the yaw control derivative N_{ped} , which decreases, and the lateral speed derivative N_v , which increases significantly in forward

flight. Both results are anticipated. A time delay of 0.099 sec is identified to account for the unmodeled high-frequency dynamics.

Heave dynamics. The heave damping derivative Z_w has the correct sign. In cruise flight, the larger heave damping and heave control sensitivity Z_{cot} are anticipated. The latter is directly related to the reduction in induced velocity in cruise flight.

Time domain verification

For the time domain verification, special flight experiments using doublet-like control inputs are performed in hover and forward flight. The recorded inputs are used as inputs to the identified model, and the model-predicted responses are compared with the recorded helicopter responses. For both the hover and cruise conditions, the results from the comparison are presented in Figs. 9 and 10, and overall, excellent agreement is achieved.

Two areas exhibit some mismatch between model-predicted and actual recorded responses: first, in the yaw rate response to the lateral cyclic input for the hover condition (Fig. 9); second, in the lateral velocity response to the directional input for the cruise condition (Fig. 10). Note that both mismatches involve the lateral directional dynamics. Furthermore, the accuracy of the identified linear model is excellent for large attitudes and large excursions from the nominal operating conditions. For example, the helicopter reaches bank angles up to 40 degrees and pitch attitudes up to 20 degrees. Note also that the cruise-flight experiments covered a range from 30 to 60 ft/sec (10 to 20 m/sec).

Eigenvalues and dynamic modes

Important dynamic characteristics of the R-50 can be understood from eigenvalues and eigenvectors computed from the identified model. Tables 6 and 7 list the eigenvalues and the dynamic modes obtained for the hover and cruise conditions.

Some of the modal characteristics can be related to the identified derivatives. For example, the frequency of the pitch and roll coupled fuselage/rotor/stabilizer modes can be related to the square root of the pitch flap spring ($\sqrt{M_a} = 9.1$ rad/sec) and the square root of the roll flap spring ($\sqrt{L_b} = 12.9$ rad/sec), respectively. Moreover, it can be shown that the small damping ratio of these modes directly reflects the large effective rotor time constant introduced by the stabilizer bar; for example, in the roll axis: $\zeta_{roll-flap} = 2\tau_s\sqrt{L_b} = 0.11$, and in the pitch axis: $\zeta_{pitch-flap} = 2\tau_s\sqrt{M_a} = 0.16$.

Table 6. Eigenvalues and modes in hover-flight condition

Eigenvalue	Location	Mode Description
$\lambda_{1,2}$	$0.306 \pm 0.094i$ ($\zeta = -0.96; \omega = 0.32$ rad/sec)	Unstable, damped, long period oscillatory, phugoid type mode. The main components are the longitudinal and lateral velocities and the roll and pitch angles
$\lambda_{3,4}$	$-0.401 \pm 0.086i$ ($\zeta = 0.98; \omega = 0.41$ rad/sec)	Damped, long period oscillatory, phugoid type mode. The main components are the longitudinal and lateral velocities, the vertical velocity, and the roll, pitch, and yaw angles
λ_5	-0.608	Damped yaw-heave mode
$\lambda_{6,7}$	$-1.7 \pm 8.19i$ ($\zeta = 0.20; \omega = 8.4$ rad/sec)	Lightly damped short period pitch mode. The main components are the pitch and roll rate. The mode has a 25% roll rate component. This mode is related to the coupled fuselage/rotor/stabilizer bar dynamics
$\lambda_{8,9}$	$-6.2 \pm 8.2i$ ($\zeta = 0.60; \omega = 10.3$ rad/sec)	Underdamped short period yaw mode (effect of active yaw damping)
$\lambda_{10,11}$	$-2.66 \pm 11.6i$ ($\zeta = 0.22; \omega = 11.9$ rad/sec)	Lightly damped short period roll mode. The main components are the roll rate, the yaw rate and the pitch rate. This mode is related to the coupled fuselage/rotor/stabilizer bar dynamics
$\lambda_{12,13}$	$-20.2 \pm 4.7i$ ($\zeta = 0.97; \omega = 20.7$ rad/sec)	Nearly critically damped short period oscillatory roll mode. The main components are the roll and pitch (40%) rate. This mode is related to the coupled fuselage/rotor/stabilizer bar dynamics

Table 7. Eigenvalues and modes in cruise-flight condition

Eigenvalue Location		Mode Description
λ_1	0.122	Damped longitudinal mode
λ_2	-0.96	Damped yaw-heave mode with a component of roll motion
λ_3	-1.84	Damped lateral-directional mode
$\lambda_{4,5}$	$-2.32 \pm 8.79i$ ($\zeta = 0.26; \omega = 9.1$ rad/sec)	Lightly damped short period pitching mode with a large (90%) rolling component. This mode is related to the coupled fuselage/rotor/stabilizer bar dynamics
$\lambda_{6,7}$	$-5.0 \pm 8.13i$ ($\zeta = 0.52; \omega = 9.5$ rad/sec)	Underdamped short period yawing mode (active yaw damping effect)
$\lambda_{8,9}$	$-3.4 \pm 12.4i$ ($\zeta = 0.26; \omega = 12.9$ rad/sec)	Lightly damped short period rolling mode with a small (10%) pitching component. This mode is related to the coupled fuselage/rotor/stabilizer bar dynamics
$\lambda_{10,11}$	$-27.04 \pm 7.02i$ ($\zeta = 0.97; \omega = 27.9$ rad/sec)	Nearly critically damped short period rolling mode with a 40% pitching component

Concluding Remarks

A parameterized model of a small-scale rotorcraft dynamics was developed and successfully identified using frequency domain identification methods. The key results are:

1) A coupled fuselage-rotor model based on the hybrid model formulation, augmented to account for the presence of a stabilizer bar, allows an accurate fit of the frequency responses derived from the flight data for both hover and cruise conditions.

2) The identification results are better than what is usually attained in full-scale identification. The dynamics of the R-50 are governed by first-order effects; the rotor forces and moments dominate the dynamics.

3) The model has a minimum number of parameters. Most of which have a well defined physical meaning. This enabled the extraction of key system parameters, including the main rotor and stabilizer bar time constants τ_f and τ_s , the stabilizer bar gearings K_c and K_d , and the flapping spring derivatives L_b and M_d .

4) Time domain verification showed that the model accurately predicts the response of the helicopter to control inputs. The identified model should be well suited to flight control design, handling quality evaluation, and simulation applications.

5) The validation of the value of the key model parameters by helicopter theory demonstrates that the model is physically meaningful and should be applicable to the identification of other small-scale helicopters.

6) To improve the identification of the quasi-steady derivatives, longer flight-data sequences should be used in the future. This will require better flight test techniques for the collection of flight data in cruise conditions.

Acknowledgments

The authors are grateful to Drs. Omead Amidi, Mark DeLous and Ryan Miller for making Carnegie Mellon's R-50 available and for helping with the collection of the flight data. This work was supported by Yamaha Motor Corporation and by NASA under Grant NAG2-1276.

References

¹Tischler, M. B., and Cauffman, M. G., "Frequency-Response Method for Rotorcraft System Identification: Flight Application to BO-105 Coupled Rotor/Fuselage Dynamics," *Journal of the American Helicopter Society*, Vol. 37, (3), 1992, pp. 3-17.

²Fletcher, J. W., "Identification of UH-60 Stability Derivative Models in Hover from Flight Test Data," *Journal of the American Helicopter Society*, Vol. 40, (1), 1995.

³Morris, J., Nieuwstadt, M. V., and Bendotti, P., "Identification and Control of a Model Helicopter in Hover," Proceedings of the American Control Conference, June 1994.

⁴Bruce, P. B., Silva, J. E. F., and Kellett, M. G., "Maximum Likelihood Identification of a Rotary-Wing RPV Simulation Model From Flight-Test Data," AIAA Paper No. 98-4157, Proceedings of the AIAA Atmospheric Flight Mechanics Conference and Exhibit, Boston, MA, 1998.

⁵Amidi, O., Kanade, T., and Miller, R., "Vision-based Autonomous Helicopter Research at Carnegie Mellon Robotics Institute," Proceedings of Heli Japan '98, Japan, April 1998.

⁶Johnson, W., *Helicopter Theory*, Dover Publications, New York, NY, 1994, Chapter 15.

⁷Heffley, R. K., "Compilation and Analysis of Helicopter Handling Qualities Data; Volume I: Data Compilation," Technical Report CR-3144, NASA, 1979.

⁸Langhaar, H. L., *Dimensional Analysis and Theory of Models*, John Wiley & Sons, New York, 1951.

⁹Padfield, G. D., *Helicopter Flight Dynamics: The Theory and Application of Flying Qualities and Simulation Modeling*, AIAA Education Series, Washington, 1996, pp. 38-40.

¹⁰Ham, J. A., Gardner, G. K., and Tischler, M. B., "Flight-Testing and Frequency-Domain Analysis for Rotorcraft Handling Qualities," *Journal of the American Helicopter Society*, Vol. 40, (2), 1995, pp. 28-38.

¹¹Tomashofski, C. A., and Tischler, M. B., "Flight Test Identification of SH-2G Dynamics in Support of Digital Flight Control System Development," American Helicopter Society 55th Annual Forum Proceedings, Montreal, Canada, May 1999.

¹²Bendat, J. S., and Piersol, A. G., *Engineering Applications of Correlation and Spectral Analysis*, John Wiley & Sons., New York, NY, 1993, pp. 43-77.

¹³Hansen, R. S., "Toward a Better Understanding of Helicopter Stability Derivatives," *Journal of the American Helicopter Society*, Vol. 29, (1), 1982, pp. 15-24.

¹⁴Chen, R., "Effects of Primary Rotor Parameters on Flapping Dynamics," Technical Report TP-1431, NASA, 1980.

¹⁵Mettler, B., Tischler, M. B., and Kanade, T., "System Identification of Small-Size Unmanned Helicopter Dynamics," American Helicopter Society 55th Annual Forum Proceedings, Montreal, Canada, May 1999.